

# A Discontinuous Galerkin Method for Two-Temperature Plasmas

Guang Lin and George Em Karniadakis \*

Division of Applied Mathematics

Brown University

March 11, 2005

## Abstract

We develop a formulation for the single-fluid/two-temperature equations for simulating two-species, compressible, non-equilibrium plasma flows. The divergence-free condition of the magnetic field is enforced via the characteristic decomposition of an extended nine-wave system. The source terms are modified appropriately to improve energy and momentum conservation accuracy. A spectral/ $hp$  element algorithm is employed in the discretization combined with a discontinuous Galerkin formulation for the advective and diffusive contributions. The formulation is conservative, and monotonicity is enforced by appropriately lowering the spectral order around discontinuities. A new MHD flux introduced here is the MHD-HLLC (Harten-Lax-van Leer Contact wave) flux that preserves monotonicity and resolves contact discontinuity better. Exponential convergence is demonstrated for a magneto-hydrostatic problem. Two tests are presented using the new MHD-HLLC flux. Also, the differences between the single-temperature and the two-temperature models are presented for two-dimensional plasma flows around bluff bodies are simulated.

---

\*Corresponding author, gk@dam.brown.edu

Report Documentation Page				Form Approved OMB No. 0704-0188	
Public reporting burden for the collection of information is estimated to average 1 hour per response, including the time for reviewing instructions, searching existing data sources, gathering and maintaining the data needed, and completing and reviewing the collection of information. Send comments regarding this burden estimate or any other aspect of this collection of information, including suggestions for reducing this burden, to Washington Headquarters Services, Directorate for Information Operations and Reports, 1215 Jefferson Davis Highway, Suite 1204, Arlington VA 22202-4302. Respondents should be aware that notwithstanding any other provision of law, no person shall be subject to a penalty for failing to comply with a collection of information if it does not display a currently valid OMB control number.					
1. REPORT DATE <b>11 MAR 2005</b>		2. REPORT TYPE		3. DATES COVERED <b>00-03-2005 to 00-03-2005</b>	
4. TITLE AND SUBTITLE <b>A Discontinuous Galerkin Method for Two-Temperature Plasmas</b>				5a. CONTRACT NUMBER	
				5b. GRANT NUMBER	
				5c. PROGRAM ELEMENT NUMBER	
6. AUTHOR(S)				5d. PROJECT NUMBER	
				5e. TASK NUMBER	
				5f. WORK UNIT NUMBER	
7. PERFORMING ORGANIZATION NAME(S) AND ADDRESS(ES) <b>Brown University, Division of Applied Mathematics, 182 George Street, Providence, RI, 02912</b>				8. PERFORMING ORGANIZATION REPORT NUMBER	
9. SPONSORING/MONITORING AGENCY NAME(S) AND ADDRESS(ES)				10. SPONSOR/MONITOR'S ACRONYM(S)	
				11. SPONSOR/MONITOR'S REPORT NUMBER(S)	
12. DISTRIBUTION/AVAILABILITY STATEMENT <b>Approved for public release; distribution unlimited</b>					
13. SUPPLEMENTARY NOTES					
14. ABSTRACT					
15. SUBJECT TERMS					
16. SECURITY CLASSIFICATION OF:			17. LIMITATION OF ABSTRACT	18. NUMBER OF PAGES <b>36</b>	19a. NAME OF RESPONSIBLE PERSON
a. REPORT <b>unclassified</b>	b. ABSTRACT <b>unclassified</b>	c. THIS PAGE <b>unclassified</b>			

# 1 Introduction

Plasmas can be modelled accurately using kinetic theory, especially partially ionized plasmas. However, this involves solutions of the seven-dimensional Boltzmann equation coupled with Maxwell's equations, which is prohibitively expensive. Particle based methods, such as DSMC, are possible alternatives but for efficiency they need to be coupled with continuum fluid equations. Such hybrid methodologies have been used successfully recently in the simulation of ion thruster plumes, but hybrid kinetic-continuum methods are still under development [1, 2], and open issues with the DSMC remain the treatment of electrons as well as the modelling of charged particle collisions.

Continuum-based, i.e. purely fluid approaches, have been successful in describing the macroscopic features of high density plasmas in many diverse applications [3, 4, 5, 6, 7, 8, 9, 10]. They are derived from the Boltzmann equation by taking appropriate moments for each species. The standard mathematical description is that of single-fluid MHD with magnetic and gas dynamic viscous effects. However, a single-fluid MHD description has its limitations as it cannot account for local thermodynamic non-equilibrium effects and cannot consider non-neutral regions and sheath interactions. To this end, two-fluid plasma models [11] and corresponding solvers have been under development more recently [12]. They can overcome certain limitations of the single-fluid MHD model such as the Hall effect and diamagnetic terms, which model contributions to ion current and the finite Larmor radius of the plasma constituents. However, they still assume local thermodynamic equilibrium within each fluid. From the computational standpoint, the two-fluid model is much more complex system to solve, especially for large values of the Hall parameter, and approximate Riemann solvers are still under development [12].

In between the single-fluid and the two-fluid models for plasmas is the *two-temperature model*. It can account partially for the energy transfer between heavy species and electrons, and it is computationally more tractable. There can be many applications for which the electron temperature differs from the heavy particle temperature [13, 14, 15]. For example, experiments in [13] with boundary layers of pure NaK seeded argon showed that the electron temperature was considerably higher than the gas temperature. Moreover, the electrical conductivity and other transport coefficients in the conservation laws depend strongly on the electron temperature. This is also true for emerging applications in microfluidics, such as micro-pulsed plasma thrusters

(micro-PPTs) where viscous effects dominate, and the flow may be in a transitional state.

The objective of the current work is to develop robust high-order algorithms for a single-fluid/two-temperature plasma extending our previous work on the standard MHD model [16]. The use of high-order accuracy addresses effectively the small-scale requirements of compressible MHD turbulence [17], as well as the extra resolution required in long-time integration [18]. In addition to our work, other recent efforts to develop effective high-order methods for plasma flows have been reported in [19, 20, 21].

Discontinuous Galerkin methods [22] address two of the main difficulties in employing *high-order discretization* for the solution of hyperbolic conservation laws are:

1. Maintaining monotonicity for non-smooth solutions, and
2. preserving conservativity.

In the MHD framework, such difficulties are compounded by the imposition of the *divergence-free* condition for the magnetic field, which results in a loss of the hyperbolicity of the ideal MHD equations. This condition has been dealt with by employing staggered grids in the work of Evans & Hawley [23], which was extended by Peterkin et al. [5]. However, such an approach cannot be easily incorporated in high-order discretizations. Alternative approaches include the operator-splitting algorithm proposed by Zachary, Malagoli & Colella [4] and the development of extended Riemann solvers by Powell [6]; the latter is easily extended to multi-dimensions and also to high-order discretization. In some approaches, the divergence-free condition is not imposed directly during time-stepping but the initial conditions are projected in the divergence-free space. Assuming that the *flux* of divergence of the magnetic field satisfies a homogeneous discrete parabolic equation with homogeneous boundary conditions, then this will lead to zero discrete divergence at all times. However, in practice, discretization errors or other inconsistencies may trigger large divergence errors for such cases.

In this paper we extend the approximate Riemman solver of Powell [6] to a *nine-wave system* to account for the divergence-free condition and the extra electron energy equation. Compared to the Riemann solver [6] and also our previous work in [16], here we modify the source terms to preserve conservativity and enhance accuracy. We employ a spectral/*hp* element discretization [24] based on tensor-product polymorphic elements for the mesh

macro-skeleton. The spectral order of the Jacobi polynomials in the trial basis is variable in order to accommodate different solution requirements, i.e. low-order for shock capturing or high-order boundary layer resolution.

To preserve pressure positivity, a MHD-HLLC flux [25] is implemented in the discontinuous Galerkin method for solving compressible plasma flows. In addition to capturing the effects of contact waves, the MHD-HLLC flux also resolves Alfvén and slow waves better than the HLL (Harten-Lax-van Leer) flux and the Lax-Friedrichs flux.

As a model problem we use plasma flow past a cylinder. Depending on the specific conditions, we find that the electron temperature can be substantially different than the temperature of ions, and correspondingly this may affect the velocity field. To appreciate the differences we compare the two-temperature model with the standard MHD model under the same wall thermal condition.

The paper is organized as follows: In section 2 we present the formulation and briefly summarize details of the implementation. In section 3, we first test the convergence rate of the algorithm for an analytical problem. We then present tests using the new MHD-HLLC flux, and subsequently we simulate plasma flow past a cylinder in the subsonic and supersonic regimes. Finally, we conclude in section 4 with a few remarks.

## 2 TWO-TEMPERATURE PLASMA EQUATIONS

### 2.1 Governing Equations

The non-dimensional governing equations for single-fluid/two-temperature plasma for compressible magneto-hydrodynamics (MHD) can be expressed in conservative form as (see derivation in Appendix B):

1. *Mass Conservation:*

$$\frac{\partial \rho}{\partial t} = -\nabla \cdot (\rho \mathbf{v}) \quad (1)$$

2. *Momentum Conservation:*

$$\frac{\partial(\rho \mathbf{v})}{\partial t} = -\nabla \cdot (\rho \mathbf{v} \mathbf{v}^t - \mathbf{B} \mathbf{B}^t + (p + \frac{1}{2} |\mathbf{B}|^2) \mathbf{I} - \frac{1}{S_{vi}} \tau_i - \frac{1}{S_{ve}} \tau_e) \quad (2)$$

3. *Magnetic Field:*

$$\frac{\partial \mathbf{B}}{\partial t} = -\nabla \times (\mathbf{B} \times \mathbf{v} + \frac{1}{S_r} \nabla \times \mathbf{B}) \quad (3)$$

4. *Total Energy Conservation:*

$$\begin{aligned} \frac{\partial E_{tot}}{\partial t} = & -\nabla \cdot [(E_{tot} + p)\mathbf{v} + (\frac{1}{2}|\mathbf{B}|^2\mathbf{I} - \mathbf{B}\mathbf{B}^t) \cdot \mathbf{v} - \frac{1}{S_{vi}}\mathbf{v} \cdot \tau_i - \frac{1}{S_{ve}}\mathbf{v} \cdot \tau_e \\ & + \frac{1}{S_r}(\mathbf{B} \cdot \nabla \mathbf{B} - \nabla(\frac{1}{2}|\mathbf{B}|^2)) - \frac{\gamma}{S_{ve}Pr_e}\nabla T_e - \frac{\gamma}{S_{vi}Pr_i}\nabla T_i] \end{aligned} \quad (4)$$

5. *Electron Internal Energy Conservation:*

$$\begin{aligned} \frac{\partial \epsilon_e}{\partial t} = & -\nabla \cdot [(\epsilon_e + p_e)\mathbf{v} - \frac{\gamma}{S_{ve}Pr_e}\nabla T_e] \\ & + \mathbf{v} \cdot \nabla p_e + \frac{1}{S_{ve}}\tau_e : \nabla \mathbf{v} + \frac{1}{S_r}(\nabla \times \mathbf{B}) \cdot (\nabla \times \mathbf{B}) \end{aligned} \quad (5)$$

6. *Magnetic Flux Constraint:*

$$\nabla \cdot \mathbf{B} = 0 \quad (6)$$

7. *Ohm's Law:*

$$\mathbf{E} = \eta \mathbf{J} - \mathbf{v} \times \mathbf{B} \quad (7)$$

Here we define:

$$E_{tot} = \frac{p}{(\gamma - 1)} + \frac{1}{2}(\rho \mathbf{v} \cdot \mathbf{v} + \mathbf{B} \cdot \mathbf{B}), \quad p = p_i + p_e, \quad \epsilon_e = \frac{P_e}{\gamma - 1} \quad (8)$$

The stress tensor for ions and electrons is defined as:

$$\tau_i = (\partial_j \mathbf{v}_{ii} + \partial_i \mathbf{v}_{ij}) - \frac{2}{3} \nabla \cdot \mathbf{v}_i \delta_{ij}, \quad \tau_e = (\partial_j \mathbf{v}_{ei} + \partial_i \mathbf{v}_{ej}) - \frac{2}{3} \nabla \cdot \mathbf{v}_e \delta_{ij} \quad (9)$$

All other parameters are as defined in table 1. The subscript ‘i’ denotes ions while the subscript ‘e’ denotes electrons.

The above Ohm's law is simplified from the generalized Ohm's law in the limit of *small Larmor radius* approximation. The generalized Ohm's law can be expressed as:

$$\mathbf{E} = \eta \mathbf{j} + \mathbf{v} \times \mathbf{B} + \frac{\mathbf{j} \times \mathbf{B}}{ne} - \frac{\nabla p_e}{ne} \quad (10)$$

and thus

$$\frac{\mathbf{j} \times \mathbf{B}/ne}{\mathbf{v} \times \mathbf{B}} \sim \frac{\nabla p_e/ne}{\mathbf{v} \times \mathbf{B}} \sim \frac{r_{Li}}{L} \quad (11)$$

where  $r_{Li}$  is the ion Larmor radius and  $L$  is the scale-length of the fluid motion. We conclude that the second and third terms on the right-hand-side of equation (10) can be neglected if the ion Larmor radius is very small compared to the characteristic length scale of the fluid motion, i.e.,  $r_{Li}/L \ll 1$ . Specifically, when we consider the length scale of the fluid motion to be very small and close to the ion Larmor radius, then we have to include the two additional terms in equation (10) and use the generalized Ohm's law instead.

Alternatively, in flux form, the above conservation equations can be expressed compactly as

$$\frac{\partial \mathbf{U}}{\partial t} = -\frac{\partial \mathbf{F}_x^{Ideal}}{\partial x} - \frac{\partial \mathbf{F}_y^{Ideal}}{\partial y} - \frac{\partial \mathbf{F}_z^{Ideal}}{\partial z} \quad (12)$$

$$+ \frac{\partial \mathbf{F}_x^{Visc}}{\partial x} + \frac{\partial \mathbf{F}_y^{Visc}}{\partial y} + \frac{\partial \mathbf{F}_z^{Visc}}{\partial z} + S_{MHD} \quad (13)$$

where all flux and source terms are defined in detail in the Appendix A. The state vector is defined as:  $\mathbf{U} = (\rho, \rho u, \rho v, \rho w, B_x, B_y, B_z, E_{tot}, \epsilon_e)$

## 2.2 The $\nabla \cdot \mathbf{B} = 0$ Constraint

The presence of the  $\nabla \cdot \mathbf{B} = 0$  constraint implies that the equations do not have a strictly hyperbolic character. It has been shown in [26] that even a small divergence in the magnetic fields can dramatically change the character of results from numerical simulations. In our work, we adopt an approach which was developed originally by Powell in [6]. The idea is to re-formulate the Jacobian matrix to include a “ninth-wave”, i.e., the divergent mode that corresponds to velocity  $u$ . This way the degeneracy associated with the divergence-free condition is avoided while the rest of the eigenvalues of the Jacobian remain the same.

The primitive Jacobian matrix  $A_p$  for *single-fluid/one-temperature equations* has the form, in three-dimensions,

$$A_p = \begin{bmatrix} u & \rho & 0 & 0 & 0 & 0 & 0 & 0 \\ 0 & u & 0 & 0 & -\frac{B_x}{\rho} & \frac{B_y}{\rho} & \frac{B_z}{\rho} & \frac{1}{\rho} \\ 0 & 0 & u & 0 & -\frac{B_y}{\rho} & \frac{B_x}{\rho} & 0 & \frac{1}{\rho} \\ 0 & 0 & 0 & u & -\frac{B_z}{\rho} & 0 & \frac{B_x}{\rho} & 0 \\ 0 & 0 & 0 & 0 & 0 & 0 & 0 & 0 \\ 0 & B_y & -B_x & 0 & -v & u & 0 & 0 \\ 0 & B_z & 0 & -B_x & -w & 0 & u & 0 \\ 0 & \gamma p & 0 & 0 & -(\gamma - 1)\mathbf{u} \cdot \mathbf{B} & 0 & 0 & u \end{bmatrix}$$

Considering that  $p = p_i + p_e$ , then the primitive Jacobian matrix  $A_p$  for *single-fluid/two-temperature equations* in three-dimensions can be described, i.e.

$$A_p = \begin{bmatrix} u & \rho & 0 & 0 & 0 & 0 & 0 & 0 & 0 \\ 0 & u & 0 & 0 & -\frac{B_x}{\rho} & \frac{B_y}{\rho} & \frac{B_z}{\rho} & \frac{1}{\rho} & 0 \\ 0 & 0 & u & 0 & -\frac{B_y}{\rho} & \frac{B_x}{\rho} & 0 & \frac{1}{\rho} & 0 \\ 0 & 0 & 0 & u & -\frac{B_z}{\rho} & 0 & \frac{B_x}{\rho} & 0 & 0 \\ 0 & 0 & 0 & 0 & 0 & 0 & 0 & 0 & 0 \\ 0 & B_y & -B_x & 0 & -v & u & 0 & 0 & 0 \\ 0 & B_z & 0 & -B_x & -w & 0 & u & 0 & 0 \\ 0 & \gamma p & 0 & 0 & -(\gamma - 1)\mathbf{u} \cdot \mathbf{B} & 0 & 0 & u & 0 \\ 0 & \gamma p_e & 0 & 0 & 0 & 0 & 0 & 0 & u \end{bmatrix}$$

To modify the governing equations so as to make  $A_p$  non-singular, using Powell's criteria presented in [6],  $A_p$  is modified to be  $A'_p$ :

$$A'_p = \begin{bmatrix} u & \rho & 0 & 0 & 0 & 0 & 0 & 0 & 0 \\ 0 & u & 0 & 0 & 0 & \frac{B_y}{\rho} & \frac{B_z}{\rho} & \frac{1}{\rho} & 0 \\ 0 & 0 & u & 0 & 0 & \frac{B_x}{\rho} & 0 & \frac{1}{\rho} & 0 \\ 0 & 0 & 0 & u & 0 & 0 & \frac{B_x}{\rho} & 0 & 0 \\ 0 & 0 & 0 & 0 & u & 0 & 0 & 0 & 0 \\ 0 & B_y & -B_x & 0 & 0 & u & 0 & 0 & 0 \\ 0 & B_z & 0 & -B_x & 0 & 0 & u & 0 & 0 \\ 0 & \gamma p & 0 & 0 & 0 & 0 & 0 & u & 0 \\ 0 & \gamma p_e & 0 & 0 & 0 & 0 & 0 & 0 & u \end{bmatrix}$$

This modification effectively corresponds to adding a source term proportional to  $\nabla \cdot \mathbf{B}$ ,

$$\mathbf{S}_{Powell} = -(\nabla \cdot \mathbf{B})(0, B_x, B_y, B_z, u, v, w, \mathbf{u} \cdot \mathbf{B}, 0)^T$$

to the right-hand-side of all evolution equations. We note that this source term does not shift the physical solution since  $\nabla \cdot \mathbf{B}$  is imposed. However, some local accumulations may occur, especially at stagnation points for which  $v = 0$ . In these cases, it may be necessary to add the HelmHoltz projection, see [26].

Next, we show how we need to modify these source terms in order to better maintain *pressure positivity*. In solving the MHD system, the pressure is a derived variable. Specifically, it is obtained by subtracting off the kinetic energy and magnetic energy from the total energy. However, in applications of micropropulsion, magneto-spheric physics and astrophysics, the pressure can be several orders of magnitude smaller than either the kinetic energy or the magnetic energy. Thus, small discretization errors in the total energy can produce situations where the pressure might become negative. This leads to an unacceptable physical situation. As long as the regions in front of a magneto-sonic shock have positive pressure, negative pressures would not be produced in magneto-sonic shocks.

Janhunen [27] has reported that the solution of the Riemann problem for Powell's equations for left- and right-states with positive fluid pressures may contain unphysical intermediate state with negative fluid pressure. pressure positivity, as well as energy and momentum conservation could be regained by discarding the source terms in the energy and momentum equations, so that the source term proportional to  $\nabla \cdot \mathbf{B}$  becomes:

$$\mathbf{S} = -(\nabla \cdot \mathbf{B})(0, 0, 0, 0, u, v, w, 0, 0)^T,$$

### 2.3 Implementation of the Inviscid Terms

We evaluate the inviscid fluxes and their derivatives in the interior of the elements and add correction terms (jumps) for the discontinuities in the flux between any two adjacent elements. In order to evaluate the Euler flux at an element interface, we use an one-dimensional Riemann solver to supply an upwinded flux there, see below. At a domain boundary, we provide far field conditions and treat the exterior boundary as the boundary of a

“ghost” element. This way we can use the same Riemann solver at all element boundaries.

We linearize the one dimensional flux  $\mathbf{F}_x^{Ideal}$  in the normal direction to a shared element boundary using the *average* of the state vector at either side of the element boundary. That is, since  $\mathbf{F}_x^{Ideal}$  is a nonlinear function of the state vector, we use the average state to form an approximation to the Jacobian of the flux vector  $A_c$ .

The Jacobian matrix for the flux vector of the evolution equations expressed in primitive variables is simpler than in the conserved form. Thus, we will perform the linearization about the primitive form and transform to the conserved form. The left and right eigenvectors of the primitive Jacobian matrix  $A_p$ , similar to the results shown in [6], are:

*Entropy wave:*

$$\begin{aligned}\lambda_e &= u \\ l_e &= (1, 0, 0, 0, 0, 0, 0, -\frac{1}{a^2}, 0) \\ r_e &= (1, 0, 0, 0, 0, 0, 0, 0, 0)^t\end{aligned}$$

*Alfven Waves:*

$$\begin{aligned}\lambda_a &= u \pm \frac{B_x}{\sqrt{\rho}} \\ l_a &= \frac{1}{\sqrt{2}}(0, 0, -\beta_z, \beta_y, 0, \pm \frac{\beta_z}{\sqrt{\rho}}, \mp \frac{\beta_y}{\sqrt{\rho}}, 0, 0) \\ r_a &= \frac{1}{\sqrt{2}}(0, 0, -\beta_z, \beta_y, 0, \pm \beta_z \sqrt{\rho}, \mp \beta_y \sqrt{\rho}, 0, 0)^T\end{aligned}$$

*Fast waves:*

$$\begin{aligned}\lambda_f &= u \pm c_f \\ l_f &= \frac{1}{2a^2}(0, \pm \alpha_f c_f, \mp \alpha_s c_s \beta_x \beta_y, \mp \alpha_s c_s \beta_x \beta_z, 0, \frac{\alpha_s \beta_y a}{\sqrt{\rho}}, \frac{\alpha_s \beta_z a}{\sqrt{\rho}}, \frac{\alpha_f}{\rho}, 0) \\ r_f &= (\rho \alpha_f, \pm \alpha_f c_f, \mp \alpha_s c_s \beta_x \beta_y, \mp \alpha_s c_s \beta_x \beta_z, 0, \alpha_s \beta_y a \sqrt{\rho}, \alpha_s \beta_z a \sqrt{\rho}, \alpha_f \gamma p, \alpha_f \gamma p_e)^t\end{aligned}$$

*Slow waves:*

$$\lambda_s = u \pm c_s$$

$$\begin{aligned}
l_s &= \frac{1}{2a^2}(0, \pm\alpha_s c_s, \pm\alpha_f c_f \beta_x \beta_y, \pm\alpha_f c_f \beta_x \beta_z, 0, -\frac{\alpha_f \beta_y a}{\sqrt{\rho}}, -\frac{\alpha_f \beta_z}{\sqrt{\rho}}, \frac{\alpha_s}{\rho}, 0) \\
r_s &= (\rho\alpha_s, \pm\alpha_s c_s, \pm\alpha_f c_f \beta_x \beta_y, \pm\alpha_f c_f \beta_x \beta_z, 0, -\alpha_f \beta_y a \sqrt{\rho}, -\alpha_f \beta_z a \sqrt{\rho}, \alpha_s \gamma p, \alpha_s \gamma p_e)^t
\end{aligned}$$

Compared to [6], we have an extra wave which corresponds to the electron energy:

$$\begin{aligned}
l_{ee} &= (0, 0, 0, 0, 0, 0, 0, 0, 1) \\
r_{ee} &= (-\frac{\gamma p_e}{\rho}, 0, 0, 0, 0, 0, 0, 0, 1)^t
\end{aligned}$$

Here:

$$\begin{aligned}
(a^*)^2 &= \frac{\gamma p + \mathbf{B} \cdot \mathbf{B}}{\rho} \\
c_f^2 &= \frac{1}{2} \left( (a^*)^2 + \sqrt{(a^*)^4 - 4 \frac{\gamma p B_x^2}{\rho^2}} \right), \quad c_s^2 = \frac{1}{2} \left( (a^*)^2 - \sqrt{(a^*)^4 - 4 \frac{\gamma p B_x^2}{\rho^2}} \right) \\
\alpha_f^2 &= \frac{a^2 - c_s^2}{c_f^2 - c_s^2}, \quad \alpha_s^2 = \frac{c_f^2 - a^2}{c_f^2 - c_s^2} \\
\beta_x &= \text{sgn}(B_x), \quad \beta_y = \frac{B_y}{\sqrt{B_y^2 + B_z^2}}, \quad \beta_z = \frac{B_z}{\sqrt{B_y^2 + B_z^2}}.
\end{aligned}$$

We can transform between the primitive variables  $\mathbf{W}$  and conserved variables  $\mathbf{U}$  with the following transform:

$$A_c = \frac{\partial \mathbf{U}}{\partial \mathbf{W}} A_p \frac{\partial \mathbf{W}}{\partial \mathbf{U}}$$

where

$$\mathbf{U} = (\rho, \rho u, \rho v, \rho w, B_x, B_y, B_z, E_{tot}, \rho \epsilon_e)$$

are the *conserved variables*, and

$$\mathbf{W} = (\rho, u, v, w, B_x, B_y, B_z, p, p_e)$$

are the *primitive variables*. This gives:

$$\frac{\partial \mathbf{U}}{\partial \mathbf{W}} = \begin{bmatrix} 1 & 0 & 0 & 0 & 0 & 0 & 0 & 0 & 0 \\ u & \rho & 0 & 0 & 0 & 0 & 0 & 0 & 0 \\ v & 0 & \rho & 0 & 0 & 0 & 0 & 0 & 0 \\ w & 0 & 0 & \rho & 0 & 0 & 0 & 0 & 0 \\ 0 & 0 & 0 & 0 & 1 & 0 & 0 & 0 & 0 \\ 0 & 0 & 0 & 0 & 0 & 1 & 0 & 0 & 0 \\ 0 & 0 & 0 & 0 & 0 & 0 & 1 & 0 & 0 \\ \frac{\mathbf{u} \cdot \mathbf{u}}{2} & \rho u & \rho v & \rho w & B_x & B_y & B_z & \frac{1}{\gamma-1} & 0 \\ 0 & 0 & 0 & 0 & 0 & 0 & 0 & 0 & \frac{1}{\gamma-1} \end{bmatrix}$$

and

$$\frac{\partial \mathbf{W}}{\partial \mathbf{U}} = \begin{bmatrix} 1 & 0 & 0 & 0 & 0 & 0 & 0 & 0 & 0 \\ -\frac{u}{\rho} & \frac{1}{\rho} & 0 & 0 & 0 & 0 & 0 & 0 & 0 \\ -\frac{v}{\rho} & 0 & \frac{1}{\rho} & 0 & 0 & 0 & 0 & 0 & 0 \\ -\frac{w}{\rho} & 0 & 0 & \frac{1}{\rho} & 0 & 0 & 0 & 0 & 0 \\ 0 & 0 & 0 & 0 & 1 & 0 & 0 & 0 & 0 \\ 0 & 0 & 0 & 0 & 0 & 1 & 0 & 0 & 0 \\ 0 & 0 & 0 & 0 & 0 & 0 & 1 & 0 & 0 \\ \frac{\bar{\gamma}}{2} \mathbf{u} \cdot \mathbf{u} & -\bar{\gamma} u & -\bar{\gamma} v & -\bar{\gamma} w & -\bar{\gamma} B_x & -\bar{\gamma} B_y & -\bar{\gamma} B_z & \bar{\gamma} & 0 \\ 0 & 0 & 0 & 0 & 0 & 0 & 0 & 0 & \bar{\gamma} \end{bmatrix}$$

where  $\bar{\gamma} = \gamma - 1$ .

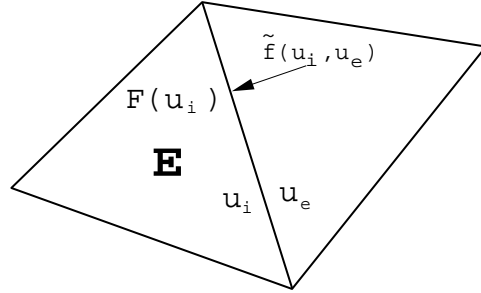


Figure 1: Interface conditions between two adjacent triangles.

We are now in a position to evaluate different fluxes at the element boundaries. The formulations of different fluxes we employ are:

1. Flux employed in [28]:

$$\begin{aligned}\hat{\mathbf{F}}_{upwind}(\mathbf{U}_I, \mathbf{U}_E) &= \frac{1}{2}[\mathbf{F}(\mathbf{U}_I) + \mathbf{F}(\mathbf{U}_E) - \frac{\partial \mathbf{U}}{\partial \mathbf{W}} \sum_{k=1}^{k=9} \alpha_k |\lambda_k| \mathbf{r}_k] \quad (14) \\ \alpha_k &= \mathbf{l}_k \cdot \frac{\partial \mathbf{W}}{\partial \mathbf{U}} (\mathbf{U}_E - \mathbf{U}_I),\end{aligned}$$

2. Lax-Friedrichs flux:

$$\hat{\mathbf{F}}_{Lax-Friedrichs}(\mathbf{U}_I, \mathbf{U}_E) = \frac{1}{2}[\mathbf{F}(\mathbf{U}_I) + \mathbf{F}(\mathbf{U}_E) - D_{max}(\mathbf{U}_E - \mathbf{U}_I)] \quad (15)$$

where  $D_{max} = \max(|\lambda_k|)$  - maximal absolute value of the eigenvalues, ‘I’ denotes interior and ‘E’ denotes exterior of the element (see figure 1). Here, the  $\mathbf{l}_k$  and  $\mathbf{r}_k$  are the ordered *left* and *right* eigenvectors of the *primitive Jacobian matrix*. We have to apply the  $\frac{\partial \mathbf{U}}{\partial \mathbf{W}}$  operator to the right eigenvectors to calculate the conserved flux. The  $\lambda'_k$ s are the wave speeds associated with the eigenvectors.

A new MHD flux introduced here is based on the MHD-HLLC flux presented in [25] that can preserve positivity and improve resolution, especially at contact interfaces.

3. MHD-HLLC interface flux:

$$\hat{\mathbf{F}}_{HLLC}(\mathbf{U}_I, \mathbf{U}_E) = \begin{cases} \mathbf{F}_I & \text{if } S_I > 0 \\ \mathbf{F}_I^* & \text{if } S_I \leq 0 \leq S_M \\ \mathbf{F}_E^* & \text{if } S_M \leq 0 \leq S_E \\ \mathbf{F}_E & \text{if } S_E < 0 \end{cases} \quad (16)$$

where  $\mathbf{F}_I^*$  and  $\mathbf{F}_E^*$  are defined as:

$$\begin{cases} \mathbf{F}_I^* = \mathbf{F}^* - \frac{S_I(S_E - S_M)}{(S_E - S_I)} \Delta \mathbf{U}^*, \\ \mathbf{F}_E^* = \mathbf{F}^* + \frac{S_E(S_M - S_I)}{(S_E - S_I)} \Delta \mathbf{U}^*. \end{cases} \quad (17)$$

with  $\mathbf{F}^* = \frac{S_E \mathbf{F}_I - S_I \mathbf{F}_E + S_I S_E (\mathbf{U}_E - \mathbf{U}_I)}{S_E - S_I}$  and  $\Delta \mathbf{U}^* = \mathbf{U}_E^* - \mathbf{U}_I^*$ . The wave-speeds  $S_I$ ,  $S_M$  and  $S_E$  are defined as:

$$\begin{cases} S_I = \min[\lambda_l(\mathbf{U}_I), \lambda_l(\mathbf{U}^{Roe})], \\ S_M = \frac{\rho_I v_{nI}(v_{nI} - S_I) - \rho_E v_{nE}(v_{nE} - S_E) + p_I - p_E + (|\mathbf{B}|_I^2 - |\mathbf{B}|_E^2)/2}{\rho_I(v_{nI} - S_I) - \rho_E(v_{nE} - S_E)}, \\ S_E = \min[\lambda_m(\mathbf{U}_E), \lambda_m(\mathbf{U}^{Roe})]. \end{cases} \quad (18)$$

Here  $\lambda_l(\mathbf{U}^{Roe})$  and  $\lambda_m(\mathbf{U}^{Roe})$  are the smallest and largest eigenvalues respectively, of the Roe-averaged matrix. Roe-averaged matrix  $A(\bar{\mathbf{U}})$ , which satisfies the following property:

$$\mathbf{F}(\mathbf{U}_E) - \mathbf{F}(\mathbf{U}_I) = A(\bar{\mathbf{U}})(\mathbf{U}_E - \mathbf{U}_I) \quad (19)$$

Correspondingly,  $\lambda_l(\mathbf{U}_I)$  and  $\lambda_m(\mathbf{U}_E)$  are the smallest and largest eigenvalues of the left and right states of the matrix  $A_p$ . The positivity of pressure and density using the MHD-HLLC flux has been demonstrated in [25]. Analytic results have shown that the flux resolves isolated contact discontinuities and fast waves accurately.

## 2.4 Implementation of the Viscous Terms

The viscous terms are evaluated in two steps. First, we obtain the spatial derivatives of the primitive variables using the discontinuous Galerkin approach. Then, we repeat the process for each of the viscous fluxes using these derivatives. If we employ Dirichlet boundary conditions for the momentum and energy variables, we set these terms explicitly after the fluxes have been evaluated and then project the result using the orthogonal basis. Here we use the average of the variables and fluxes at the interface. This approach leads to sub-optimal performance at low polynomial order  $p$ . However it does not make much difference at high polynomial order  $p$ . For more details, see [16].

### 3 Convergence and Simulations

#### 3.1 Convergence Test

A simple test for the compressible MHD component of the algorithm we developed is to consider a steady irrotational magnetic field and zero velocity. The test was performed as an initial value problem, and the following exact solution

$$\begin{aligned}\rho &= 1, u = 0, v = 0 \\ E &= 19.84 + \frac{e^{(-2\pi y)}}{2}, \quad E_e = 9.92 \\ B_x &= -\cos(\pi x)e^{(-\pi y)}, B_y = \sin(\pi x)e^{(-\pi y)}\end{aligned}$$

was used as the *boundary conditions* and as the *initial condition*. This solution but without the part concerning  $E_e$  was derived by Priest [29]. The irrotational magnetic field implies that the Lorentz force is zero so the momentum equations are trivially satisfied. The magneto-viscous term is zero and the  $\mathbf{v} \times \mathbf{B}$  term is also zero. Thus, the compressible single-fluid/two-temperature MHD equations are satisfied. Here, we take  $m_i = 1836m_e$  [30] and we set the interaction term  $\Phi = 0$  to make the problem simpler ( $m_i$  is the ion mass and  $m_e$  is the electron mass).

The domain and hybrid discretization we used are depicted in figure 2. We also show that the approximation error decreases exponentially with increasing expansion order for all the three forms of error considered in the  $L_\infty$ ,  $H_1$ , and  $L_2$  norms.

#### 3.2 Numerical Tests for the MHD-HLLC Interface Flux

To verify our two-dimensional discontinuous Galerkin solver with the MHD-HLLC flux, we use the one-dimensional benchmark MHD shock-tube problem developed by Brio and Wu [31]. The one-dimensional Riemann problem is given for  $x \in [-1, 1]$ :

$$\mathbf{U}_p = (\rho, u_x, u_y, u_z, B_y, B_z, p) = \begin{cases} (1.000, 0, 0, 0, +1, 0, 1.0) & \text{for } x < 0 \\ (0.125, 0, 0, 0, -1, 0, 0.1) & \text{for } x > 0 \end{cases} \quad (20)$$

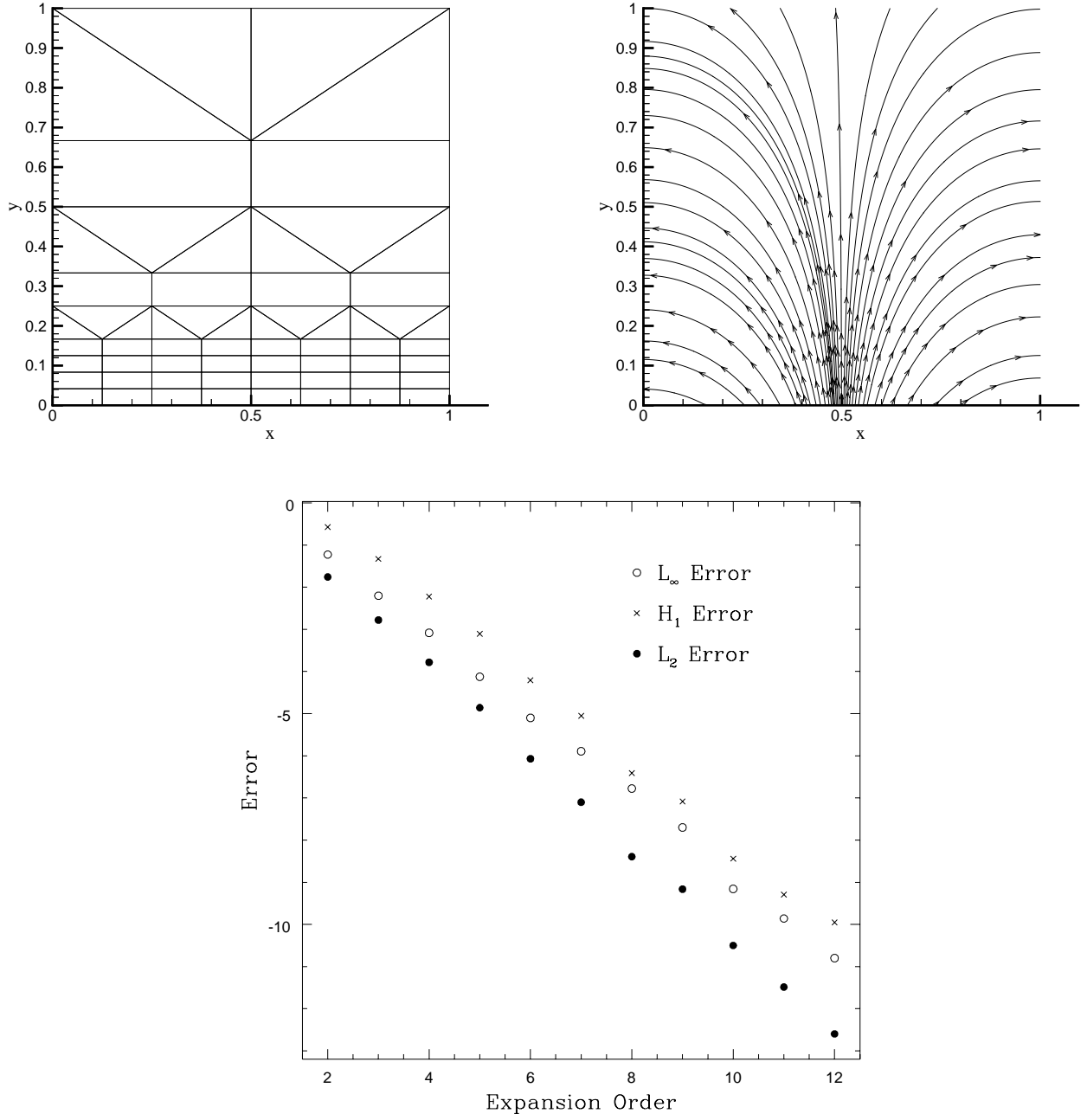


Figure 2: Magneto-hydrostatic test case. Top-Left: spectral element hybrid mesh consisting of 38 triangular elements and 22 rectangular elements. Top-Right: Magnetic streamlines of steady solution; Bottom: Dependence of steady state  $\log$ -error of magnetic field  $B_x$  on expansion spectral order.

with  $B_x = 0.75$  and  $\gamma = 2$ . The solution at  $t = 0.2$  is shown in figure 3, which includes the left-moving waves: the fast rarefaction wave, the intermediate shock attached by a slow rarefaction wave; and, the right moving waves: the contact discontinuity, a slow shock, and a fast rarefaction wave. The results are obtained by the two-dimensional discontinuous Galerkin solver on a mesh, consisting of 800 square elements. The solid line is the result using the MHD-HLLC flux, see equation (16), the dashed line is obtained using the Lax-Friedrichs flux, see equation (15). We can see the MHD-HLLC flux gives much sharper resolution, especially at the contact interface.

The second Riemann problem is given by:

$$\mathbf{U}_p = (\rho, u_x, u_y, u_z, B_y, B_z, p) = \begin{cases} (1.000, 0, 0, 0, +1, 0, 1000.0) & \text{for } x < 0 \\ (0.125, 0, 0, 0, -1, 0, 0.1) & \text{for } x > 0 \end{cases} \quad (21)$$

with  $B_x = 0$  and  $\gamma = 2$ . This problem is used to evaluate the code for high Mach number flow. If one regards the term  $p + \frac{1}{2}|B|^2$  as the “hydrodynamic pressure”, the system becomes a standard hydrodynamical Riemann problem. The computational domain is taken to be  $[-1, 1]$  with 400 square elements. The solution at  $t = 0.012$  is shown in figure 4, which shows that the MHD-HLLC flux can resolve the high Mach number waves more accurately than the Lax-Friedrichs flux.

### 3.3 Flow Past a Cylinder

Next, we consider the problem of plasma flow with uniform free stream properties past a circular cylinder. As the mass and thermal properties for electrons and ions are quite different, at the final steady state, they will have quite different temperature distributions around the cylinder. Here we consider electrons and ions having the same temperature over the cylinder surface as the free stream temperature. To simplify our calculation, we set the atomic number of ions  $Z = 1$  and  $m_i = 1836m_e$ . We perform simulations using unstructured meshes for all the subsonic and transonic cases; it is shown in figure 5 top, consisting of 490 triangular elements; the mesh used for the supersonic case is shown in figure 5 bottom, consisting of 1132 triangular elements.

h-refinement is employed around the shock, based on the following crite-

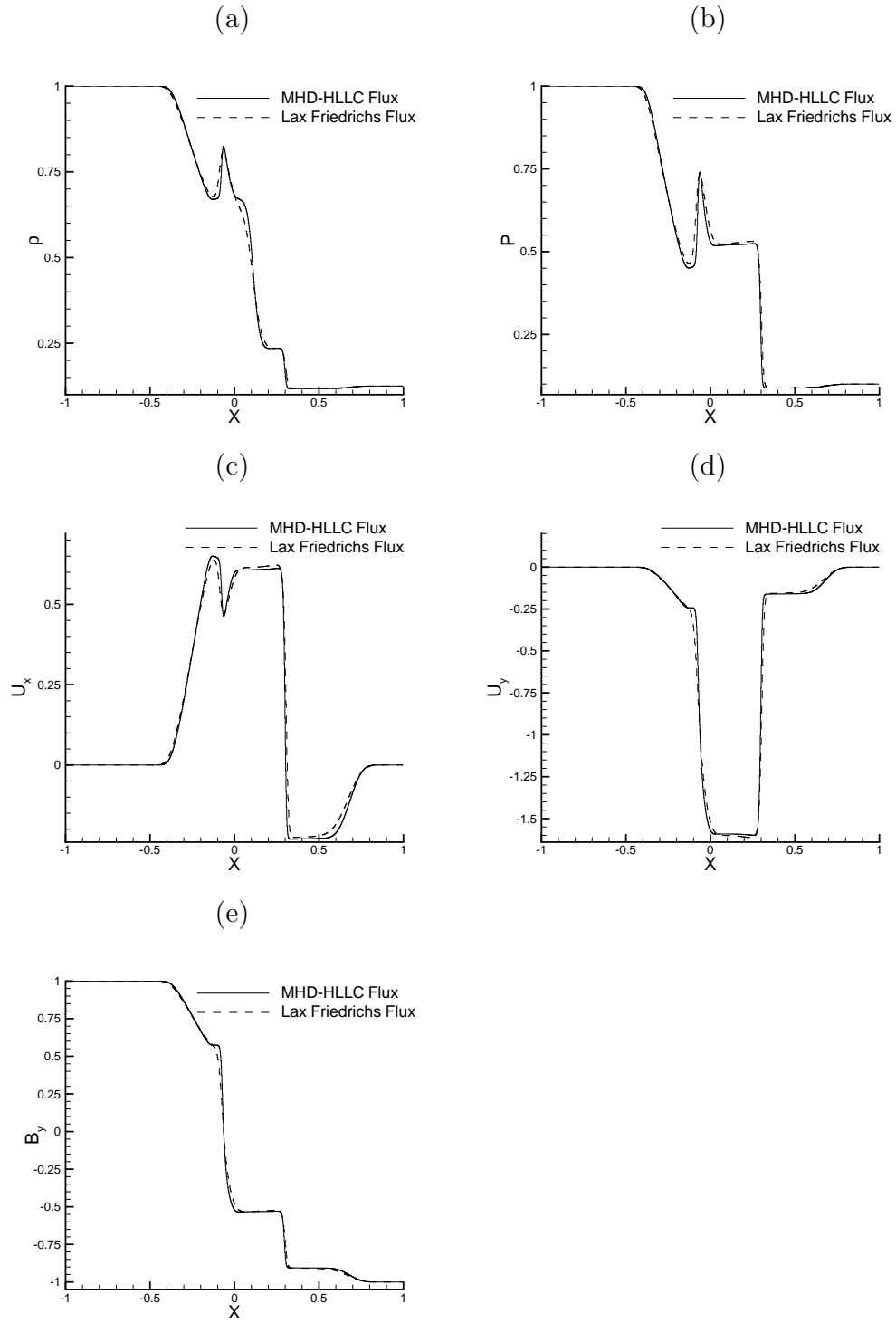


Figure 3: 1D coplanar MHD Riemann problem: Solid line: MHD-HLLC flux; Dashed line: Lax-Friedrichs flux. (a):  $\rho$ ; (b):  $p$ ; (c):  $U_x$ ; (d):  $U_y$ ; (e):  $B_y$ .

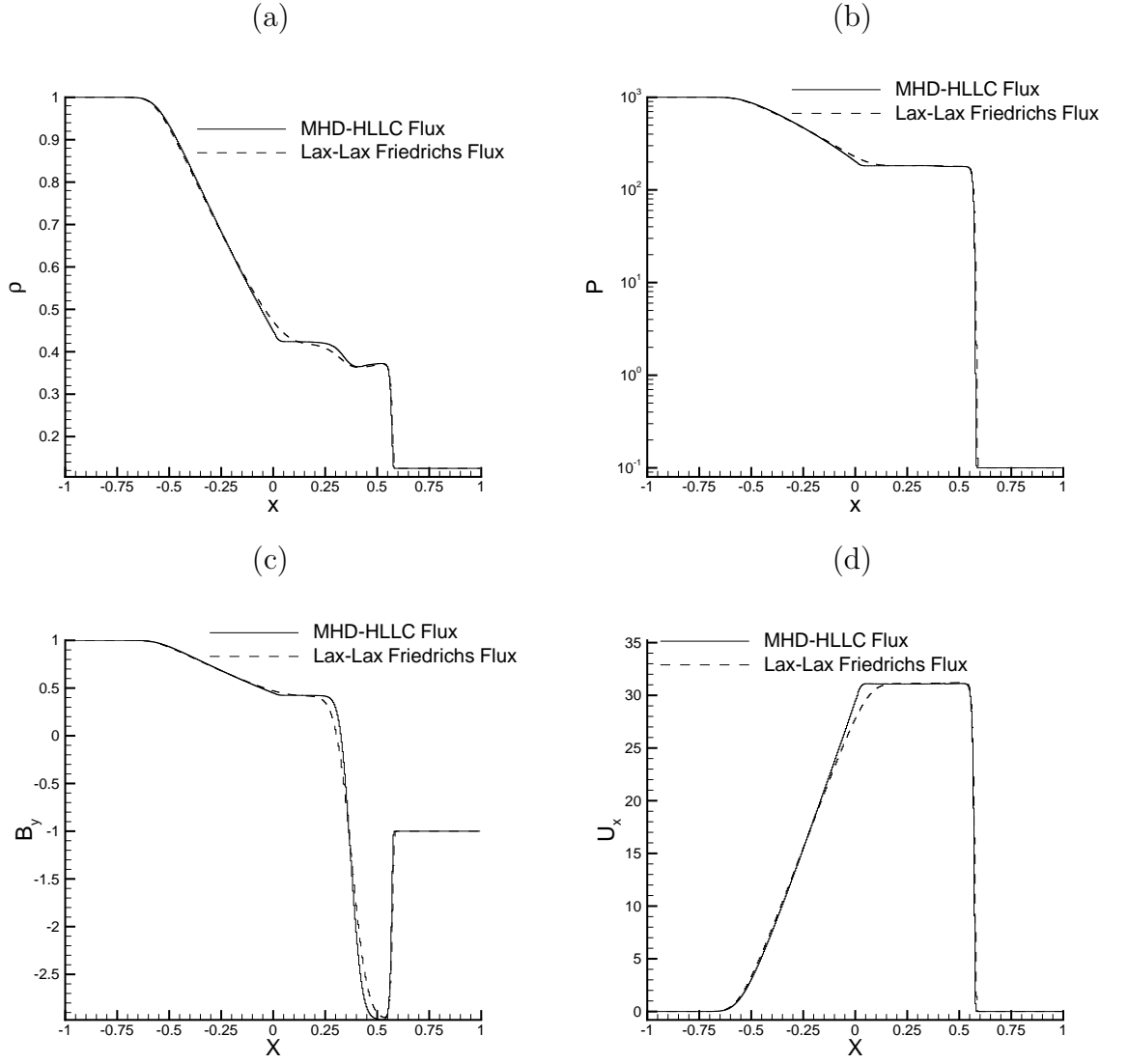


Figure 4: High Mach number Riemann problem: Solid line: MHD-HLLC flux; Dashed line: Lax-Friedrichs flux. (a):  $\rho$ ; (b):  $p$ ; (c):  $B_y$ ; (d):  $U_x$ .

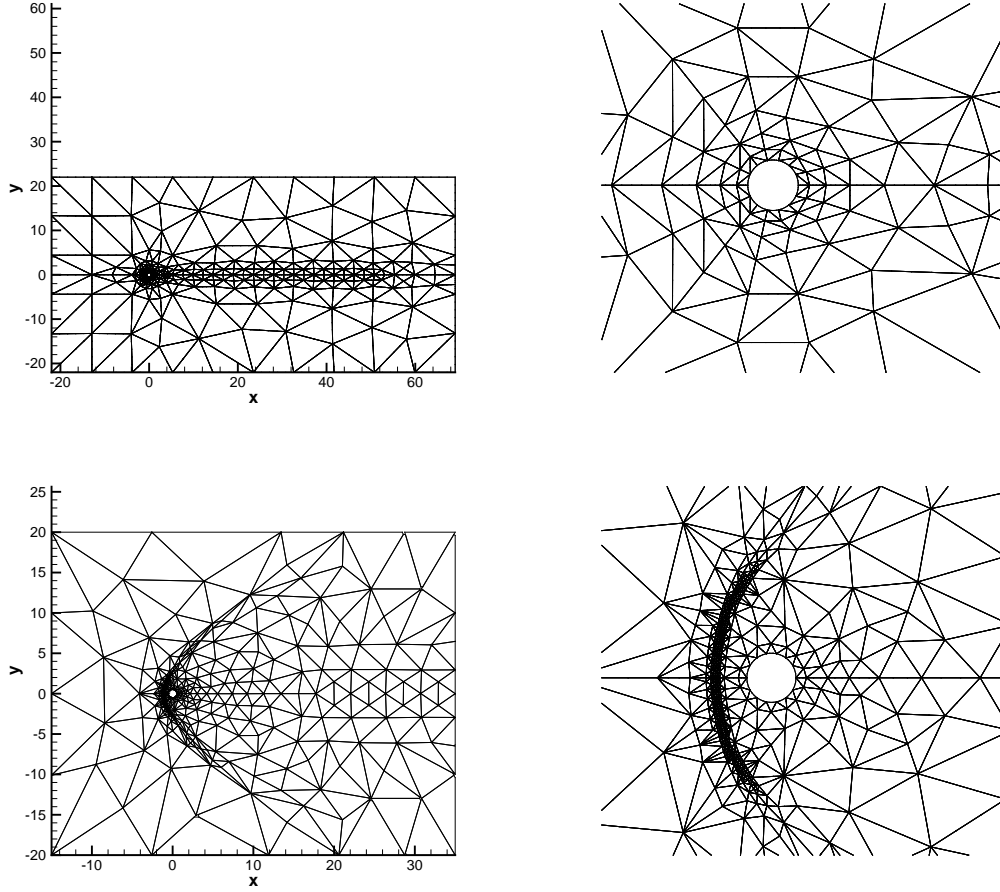


Figure 5: Top : Computational domain for plasma flow past a circular cylinder simulations at Mach number 0.7 and Reynolds number 100. Top-Left : Entire domain. Top-Right : Zoom around the cylinder. Bottom : Computational domain at Mach number 2 and Reynolds number 100. Bottom-Left : Entire domain. Bottom-Right : Zoom around the cylinder.

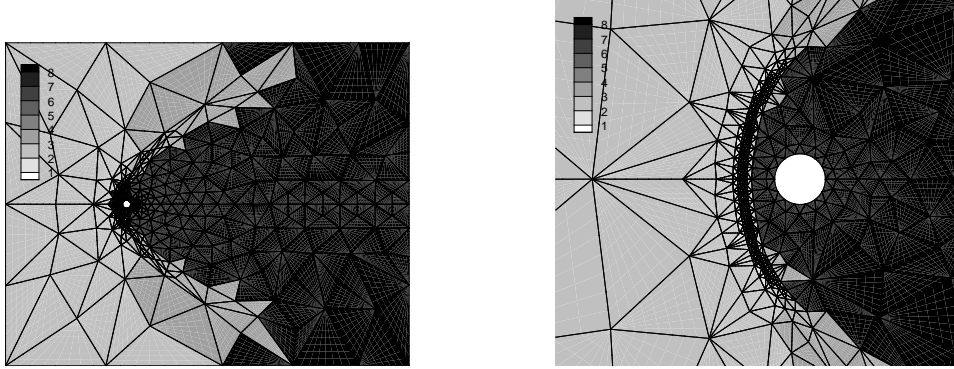


Figure 6: Left: Variable order computational domain; Right: Variable order around the cylinder.

tion (the gradient of density in the direction of the flow):

$$\nabla(\rho) \cdot \mathbf{V} > M; \quad (22)$$

where  $M$  is an adjustable parameter. The elements chosen are split into 4 smaller elements. Figure 6 plots the computational domain showing the variable polynomial order; p-refinement is used away from the shock. To preserve solution monotonicity, we lower the spectral order around discontinuities appropriately. The polynomial order  $p$  is determined based on the area of the element but more sophisticated criteria can be used to find the optimal  $p$ . Due to the stability issue, first-order schemes or limiters have to be implemented around the shock. Since limiters will give more smearing results, we prefer to use low order elements in conjunction with h-refinement close to the shock.

In all the cases, we set  $Re = 100$ ,  $B_x = 0.1$  and  $B_y = 0.0$  at the inflow, where  $B_x$  is the  $x$ -component of the magnetic field and  $B_y$  the  $y$ -component of the magnetic field. The two simulations were run with polynomial order  $p = 5$  until the flow reaches a time-periodic or a steady state; p-refinement tests have shown only very small difference in the results.

In figures 7 and 8, we plot the ion and the electron temperature contours of the instantaneous field. A von Karman vortex street develops in the subsonic regime. However, the flow is steady at supersonic states as shown in figure

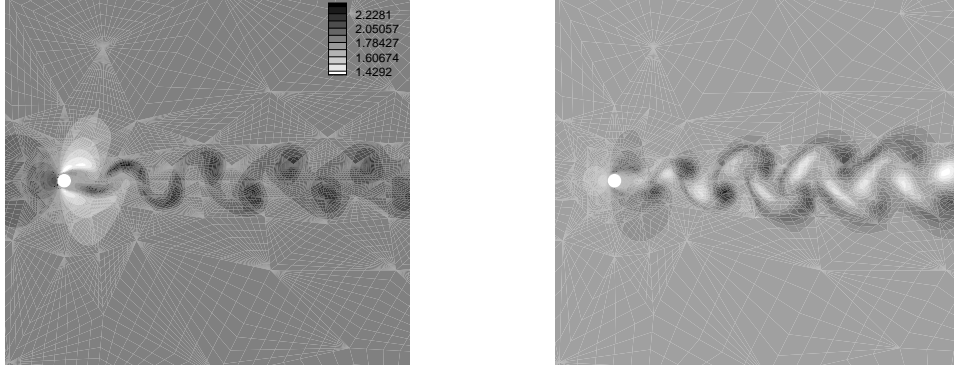


Figure 7: Instantaneous nondimensional temperature contours for flow past a circular cylinder at Mach number 0.7, Reynolds number 100 and cylinder wall temperature  $T_i = T_e = 1.8367$ . Left : Ion temperature contours. Right : Electron temperature contours.



Figure 8: Instantaneous nondimensional temperature contours for flow past a circular cylinder at Mach number 2, Reynolds number 100 and cylinder wall temperature  $T_i = T_e = 0.225$ . Left : Ion temperature contours. Right : Electron temperature contours.

8. In particular, we have performed several simulations for the compressible flow, using the one-temperature model and the two-temperature model in order to present differences in the forces and frequency.

Specifically, in order to compare the one-temperature model with the two-temperature model, we integrate the flow field over one time period and obtain the time-averaged flow field. In figures 9 and 10, we plot the time-averaged contour lines of the ion and the electron temperature using the two-temperature model and the temperature contours using the one-temperature model. Also, we present temperature profiles along a line on top of the cylinder aligned with the vertical axis, as shown in figure 11, to compare the temperature distributions. In figures 12 and 13, we plot the normal profiles of temperature in one-temperature model and profiles of the electron and the ion temperature in two-temperature model starting at the top of the cylinder at Mach number 0.7 and 2. From these figures, we can see that the results of one-temperature model are quite different from the ones of the two-temperature model. In figures 12 and 13, electrons and ions have the same temperature on the cylinder surface and the electron temperature increases while the ion temperature decreases in the direction away from the cylinder surface. From figures 9 and 12, we can see that the ion temperature is larger than the electron temperature ahead of the cylinder at Mach number 0.7. However the electron temperature is larger than the ion temperature on the two sides of cylinder. Figure 13 shows the electron temperature is smaller than the ion temperature on the two sides of cylinder at Mach number 2. Generally, temperature profiles obtained from one temperature model is similar to the ion temperature rather than the electron temperature. The relation between two temperatures model and one temperature model can be given as:  $T = \frac{T_i + T_e}{2}$ , if ions and electrons have the same number density  $n_i = n_e$ .

## 4 SUMMARY

We have developed a discontinuous Galerkin solver to model two-temperature plasmas as part of a hierarchical modelling approach and a compromise between single-temperature and two-fluids models. We have demonstrated spectral convergence for an analytical problem and also demonstrated the robustness of the method in dealing with shocks without the use of flux limiters or artificial viscosity terms. The issue of preserving positivity is addressed by introducing a new interface flux, the MHD-HLLC flux.

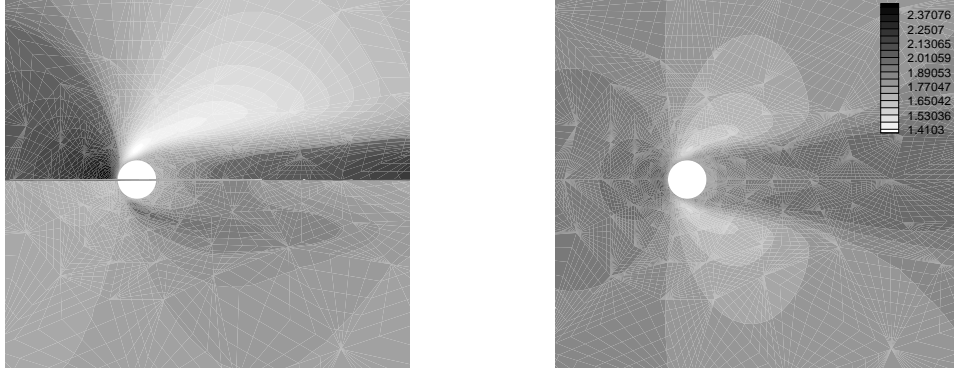


Figure 9: Left : Time average contour lines of ion nondimensional temperature (upper half plane) and electron nondimensional temperature (lower half plane) at Mach number 0.7, Reynolds number 100 and cylinder wall temperature  $T_i = T_e = 1.8367$  using the two-temperature model. Right : Time average contour lines of nondimensional temperature using the one-temperature model.

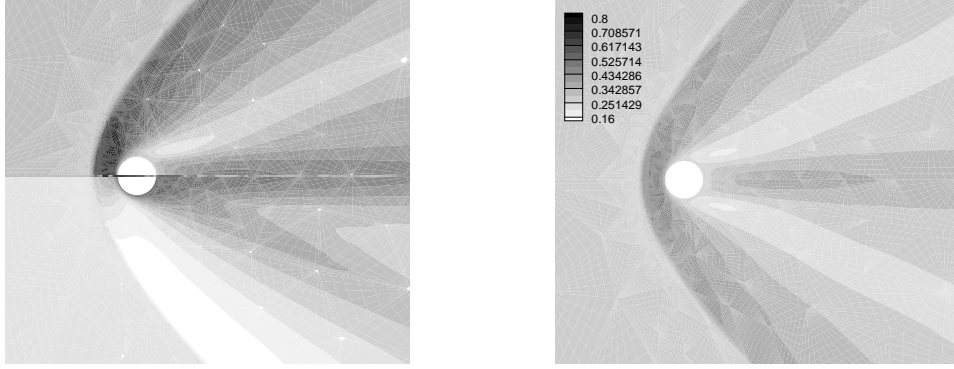


Figure 10: Left : Time average contour lines of ion nondimensional temperature (upper half plane) and electron nondimensional temperature (lower half plane) at Mach number 2, Reynolds number 100 and cylinder wall temperature  $T_i = T_e = 0.225$  using the two-temperature model; Right : Time average contour lines of nondimensional temperature using the one-temperature model.

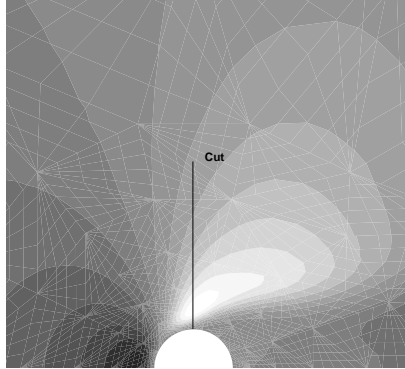


Figure 11: Location where profiles of temperature along the line shown aligned with the vertical axis are taken. Contours of ion temperature at Mach number 0.7 are shown in the background.

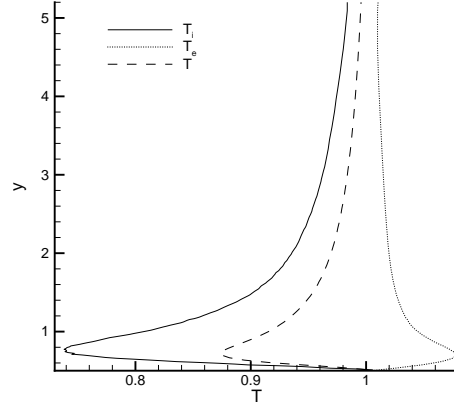


Figure 12: Normal profiles of temperature nondimensionalized by cylinder wall temperature at Mach number 0.7, Reynolds number 100 and cylinder wall temperature  $T_i = T_e = 1.8367$ . Solid line: Ion temperature from two-temperature model; Dotted line: Electron temperature from two-temperature model; Dashed line: Temperature from one-temperature model.

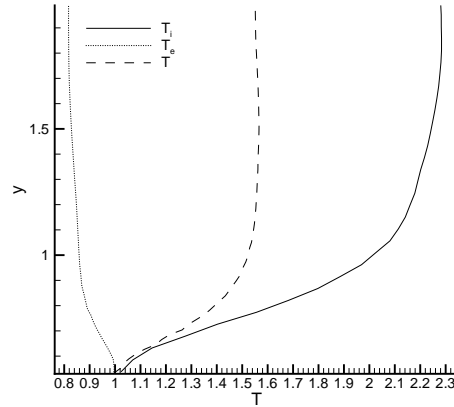


Figure 13: Normal profiles of temperature nondimensionalized by cylinder wall temperature at Mach number 2, Reynolds number 100 and cylinder wall temperature  $T_i = T_e = 0.225$ . Solid line: Ion temperature from two-temperature model; Dotted line: Electron temperature from two-temperature model; Dashed line: Temperature from one-temperature model.

Examination of contours of the divergence of the magnetic field in flow past a cylinder revealed some non-zero values in the region around the rear stagnation point. However, this was not growing in time and thus no numerical instabilities were induced even after long-time integration. This divergence field can be totally eliminated by occasional Helmholtz decomposition of the magnetic flux vector, see [16] and [26]. We are currently developing a discontinuous Galerkin method for two-fluids plasmas and we will report those results in a future publication.

## APPENDICES

### A: Detailed flux terms in single-fluid/two-temperature equations

We present here in detail the flux terms involved in the governing equations of the single-fluid/two-temperature plasma. Many of the parameters used are listed in table 1.

$$\begin{aligned}
\mathbf{F}_x^{Ideal} &= (\rho u, \rho u^2 - B_x^2 + \bar{p}, \rho uv - B_x B_y, \rho uw - B_x B_z, 0, uB_y - vB_x, uB_z - wB_x, \\
&\quad (E + \bar{p})u - (\mathbf{v} \cdot \mathbf{B})B_x, (\epsilon_e + p_e)u)^T \\
\mathbf{F}_y^{Ideal} &= (\rho v, \rho vu - B_y B_x, \rho v^2 - B_y^2 + \bar{p}, \rho vw - B_y B_z, vB_x - uB_y, 0, vB_z - wB_y, \\
&\quad (E + \bar{p})v - (\mathbf{v} \cdot \mathbf{B})B_y, (\epsilon_e + p_e)v)^T \\
\mathbf{F}_z^{Ideal} &= (\rho w, \rho wu - B_z B_x, \rho wv - B_z B_y, \rho w^2 - B_z^2 + \bar{p}, wB_x - uB_z, wB_y - vB_z, \\
&\quad 0, (E + \bar{p})w - (\mathbf{v} \cdot \mathbf{B})B_z, (\epsilon_e + p_e)w)^T \\
\mathbf{F}_x^{Visc} &= (0, \frac{2}{S_{vi}}(\frac{\partial u}{\partial x} - \frac{1}{3}\nabla \cdot \mathbf{v}), \frac{1}{S_{vi}}(\frac{\partial u}{\partial y} + \frac{\partial v}{\partial x}), \frac{1}{S_{vi}}(\frac{\partial u}{\partial z} + \frac{\partial w}{\partial x}), 0, -\frac{1}{S_r}(\frac{\partial B_y}{\partial x} - \frac{\partial B_x}{\partial y}), \\
&\quad -\frac{1}{S_r}(\frac{\partial B_z}{\partial x} - \frac{\partial B_x}{\partial z}), \frac{1}{S_{vi}}(-\frac{2}{3}(\nabla \cdot \mathbf{v})u + \mathbf{v} \cdot \nabla u + \frac{1}{2}\frac{\partial \mathbf{v}^2}{\partial x} + \frac{1}{Pr_i}\frac{\partial T_i}{\partial x} + \frac{1}{Pr_e}\frac{\partial T_e}{\partial x}) \\
&\quad + \frac{1}{S_r}(\frac{1}{2}\frac{\partial(|\mathbf{B}|^2)}{\partial x} - \mathbf{B} \cdot \nabla B_x), \frac{1}{S_{ve}Pr_e}\frac{\partial T_e}{\partial x})^T \\
\mathbf{F}_y^{Visc} &= (0, \frac{1}{S_{vi}}(\frac{\partial v}{\partial x} + \frac{\partial u}{\partial y}), \frac{2}{S_{vi}}(\frac{\partial v}{\partial y} - \frac{1}{3}\nabla \cdot \mathbf{v}), \frac{1}{S_{vi}}(\frac{\partial v}{\partial z} + \frac{\partial w}{\partial y}), -\frac{1}{S_r}(\frac{\partial B_x}{\partial y} - \frac{\partial B_y}{\partial x}), 0, \\
&\quad -\frac{1}{S_r}(\frac{\partial B_z}{\partial y} - \frac{\partial B_y}{\partial z}), \frac{1}{S_{vi}}(-\frac{2}{3}(\nabla \cdot \mathbf{v})v + \mathbf{v} \cdot \nabla v + \frac{1}{2}\frac{\partial \mathbf{v}^2}{\partial y} + \frac{1}{Pr_i}\frac{\partial T_i}{\partial y} + \frac{1}{Pr_e}\frac{\partial T_e}{\partial y}) \\
&\quad + \frac{1}{S_r}(\frac{1}{2}\frac{\partial(|\mathbf{B}|^2)}{\partial y} - \mathbf{B} \cdot \nabla B_y), \frac{1}{S_{ve}Pr_e}\frac{\partial T_e}{\partial y})^T
\end{aligned}$$

Variable	Description
$\rho(\mathbf{x}, t) = \rho_i + \rho_e$	single fluid density
$\mathbf{v}(\mathbf{x}, t) = (u, v, w)(\mathbf{x}, t)$	single fluid velocity
$\mathbf{B}(\mathbf{x}, t) = (B_x, B_y, B_z)(\mathbf{x}, t)$	magnetic fields
$E = \frac{p}{(\gamma-1)} + \frac{1}{2}(\rho \mathbf{v} \cdot \mathbf{v} + \mathbf{B} \cdot \mathbf{B})$	total energy
$p = p_i + p_e$	total pressure
$\bar{p} = p + \frac{1}{2} \mathbf{B} \cdot \mathbf{B}$	pressure plus magnetic pressure
$T_i = \frac{p_i}{\rho_i}, T_e = \frac{p_e}{\rho_e}$	ion and electron non-dimensional Temperature
$Pr_i = \frac{c_p \mu_i}{\kappa_i}, Pr_e = \frac{c_p \mu_e}{\kappa_e}$	ion and electron Prandtl Number
$\eta$	Magnetic resistivity
$\mu_i, \mu_e$	ion and electron Viscosity
$S_{vi} = \frac{\rho_0 V_A L_0}{\mu_i}, S_{ve} = \frac{\rho_0 V_A L_0}{\mu_e}$	ion and electron Viscous Lundquist number
$S_r = \frac{\mu_0 V_A L_0}{\eta}$	Resistive Lundquist number
$c_p$	Specific heat at constant pressure
$V_A^2 = \frac{\mathbf{B} \cdot \mathbf{B}}{\mu_0 \rho}$	Alfven wave speed
$A = \sqrt{\frac{V_A^2}{V_0^2}}$	Alfven Number

Table 1: Variables and parameters used in the equations of single-fluid/two-temperature compressible MHD.

$$\begin{aligned}
& + \frac{1}{S_r} \left( \frac{1}{2} \frac{\partial(|\mathbf{B}|^2)}{\partial y} - \mathbf{B} \cdot \nabla B_y \right), \frac{1}{S_{ve} Pr_e} \frac{\partial T_e}{\partial y} \Big)^T \\
\mathbf{F}_z^{Visc} = & \left( 0, \frac{1}{S_{vi}} \left( \frac{\partial w}{\partial x} + \frac{\partial u}{\partial z} \right), \frac{1}{S_{vi}} \left( \frac{\partial w}{\partial y} + \frac{\partial v}{\partial z} \right), \frac{2}{S_{vi}} \left( \frac{\partial w}{\partial z} - \frac{1}{3} \nabla \cdot \mathbf{v} \right), -\frac{1}{S_r} \left( \frac{\partial B_x}{\partial z} - \frac{\partial B_z}{\partial x} \right), \right. \\
& \left. -\frac{1}{S_r} \left( \frac{\partial B_y}{\partial z} - \frac{\partial B_z}{\partial y} \right), 0, \frac{1}{S_{vi}} \left( -\frac{2}{3} (\nabla \cdot \mathbf{v}) w + \mathbf{v} \cdot \nabla w + \frac{1}{2} \frac{\partial \mathbf{v}^2}{\partial z} + \frac{1}{Pr_i} \frac{\partial T_i}{\partial z} + \frac{1}{Pr_e} \frac{\partial T_e}{\partial z} \right) \right. \\
& \left. + \frac{1}{S_r} \left( \frac{1}{2} \frac{\partial(|\mathbf{B}|^2)}{\partial z} - \mathbf{B} \cdot \nabla B_z \right), \frac{1}{S_{ve} Pr_e} \frac{\partial T_e}{\partial z} \right)^T \\
S_{MHD} = & \left( 0, 0, 0, 0, 0, 0, 0, 0, (\mathbf{v} \cdot \nabla p_e + \frac{1}{S_{ve}} \tau_e : \nabla \mathbf{v} + \frac{1}{S_r} (\nabla \times \mathbf{B}) \cdot (\nabla \times \mathbf{B})) \right)
\end{aligned}$$

## B: From two-fluid equations to one-fluid two-temperature equations

The magnetohydrodynamic model treats the plasma as a single fluid. In the following, we derive the single-fluid/two-temperature plasma equations from the two fluids plasma equations. We denote the electron and ion masses by  $m$  and  $M$  respectively.  $n_i$  and  $n_e$  are the ion and electron number density.  $j_i, j_e, T_i, T_e, p_i, p_e$  and  $E_i, E_e$  are the current density, temperature pressure and hydrodynamic energy density of ion and electron respectively.  $E_{tot}$  and  $\epsilon_e$  are the total energy density and electron internal energy density.

We Define:

$$M = 1836n, n_i = n_e = n \quad (23)$$

$$\rho = n_i M + n_e m = n(M + m) \approx nM \quad (24)$$

$$\mathbf{j}_i = ne\mathbf{v}_i \quad (25)$$

$$\mathbf{j}_e = -ne\mathbf{v}_e \quad (26)$$

$$\mathbf{j} = ne(\mathbf{v}_i - \mathbf{v}_e) = ne(\mathbf{j}_i + \mathbf{j}_e) \quad (27)$$

$$p = p_i + p_e \quad (28)$$

$$T = \frac{T_i + T_e}{2} \quad (29)$$

$$\begin{aligned} \mathbf{v} &= \frac{n(M\mathbf{v}_i + m\mathbf{v}_e)}{\rho} \\ &= \frac{M\mathbf{v}_i + m\mathbf{v}_e}{M + m} \approx \mathbf{v}_i + \frac{m}{M}\mathbf{v}_e \approx \mathbf{v}_i \end{aligned} \quad (30)$$

$$\mathbf{v}_i \approx \mathbf{v} + \frac{m\mathbf{j}}{Mne} \approx \mathbf{v} \quad (31)$$

$$\mathbf{v}_e \approx \mathbf{v} - \frac{\mathbf{j}}{ne} \approx -\frac{\mathbf{j}}{ne} \quad (32)$$

$$E_i = \frac{nkT_i}{\gamma - 1} + \frac{1}{2}nM\mathbf{v}_i^2 \quad (33)$$

$$E_e = \frac{nkT_e}{\gamma - 1} + \frac{1}{2}nm\mathbf{v}_e^2 \quad (34)$$

$$E_{tot} = E_i + E_e + \frac{1}{2}\mathbf{B}^2 \quad (35)$$

$$\epsilon_e = \frac{nkT_e}{\gamma - 1} \quad (36)$$

where  $\gamma = 5/3$  and  $k$  is Boltzmann constant.

We make following **assumptions**:

1. *Quasineutral approximation.*

$$n = n_i = n_e \quad (37)$$

2. *High collisionality.* We assume both the electrons and ions are collision dominated. The collisions rapidly randomize the distribution function giving rise to an isotropic pressure.

3. *Small Larmor radius.*

Generalized Ohm's Law:

$$\mathbf{E} = \eta \mathbf{j} + \mathbf{v} \times \mathbf{B} + \frac{\mathbf{j} \times \mathbf{B} - \nabla p_e}{ne} \quad (38)$$

With the 'small Larmor radius' approximation, the generalized Ohm's law is simplified as:

$$\mathbf{E} = \eta \mathbf{j} - \mathbf{v} \times \mathbf{B} \quad (39)$$

4. *Electrons move much faster than ions.*

$$|\mathbf{v}_i| \ll |\mathbf{v}_e| \quad (40)$$

## Mass conservation

In two fluids plasma mass conservation equations, we have:

$$\frac{\partial n_i}{\partial t} + \nabla \cdot (n_i \mathbf{v}_i) = 0 \quad (41)$$

$$\frac{\partial n_e}{\partial t} + \nabla \cdot (n_e \mathbf{v}_e) = 0 \quad (42)$$

By Multiplying the ion and electron masses  $M$  and  $m$ , respectively, and adding above two equations together, we produce the 'single-fluid mass conservation equation',

$$\frac{\partial n(M + m)}{\partial t} + \nabla \cdot [n(M \mathbf{v}_i + m \mathbf{v}_e)] = \frac{\partial \rho}{\partial t} + \nabla \cdot (\rho \mathbf{v}) = 0 \quad (43)$$

## Momentum conservation

In two-fluids plasma, the momentum conservation equations are:

$$\begin{aligned} \frac{\partial(nM\mathbf{v}_i)}{\partial t} + \nabla \cdot (nM\mathbf{v}_i\mathbf{v}_i^t\mathbf{I}) &= -\nabla p_i + ne(\mathbf{E} + \mathbf{v}_i \times \mathbf{B}) \\ &+ \nabla \cdot (\mu_i\tau_i) \end{aligned} \quad (44)$$

$$\begin{aligned} \frac{\partial(nm\mathbf{v}_e)}{\partial t} + \nabla \cdot (nm\mathbf{v}_e\mathbf{v}_e^t\mathbf{I}) &= -\nabla p_e - ne(\mathbf{E} + \mathbf{v}_e \times \mathbf{B}) \\ &+ \nabla \cdot (\mu_e\tau_e) \end{aligned} \quad (45)$$

where  $\tau_i = (\partial_j \mathbf{v}_{ii} + \partial_i \mathbf{v}_{ij}) - \frac{2}{3} \nabla \cdot \mathbf{v}_i \delta_{ij}$  and  $\tau_e = (\partial_j \mathbf{v}_{ei} + \partial_i \mathbf{v}_{ej}) - \frac{2}{3} \nabla \cdot \mathbf{v}_e \delta_{ij}$ .

By adding the above two equations together, we have:

$$\begin{aligned} \frac{\partial(\rho\mathbf{v})}{\partial t} + \nabla \cdot (nM\mathbf{v}_i\mathbf{v}_i^t\mathbf{I} + nm\mathbf{v}_e\mathbf{v}_e^t\mathbf{I}) &\approx \frac{\partial(\rho\mathbf{v})}{\partial t} + \nabla \cdot (\rho\mathbf{v}\mathbf{v}^t\mathbf{I}) \\ &= -\nabla(p_i + p_e) + ne(\mathbf{v}_i - \mathbf{v}_e) \times \mathbf{B} + \nabla \cdot (\mu_i\tau_i + \mu_e\tau_e) \\ &= -\nabla p + \mathbf{j} \times \mathbf{B} + \nabla \cdot (\mu_i\tau_i + \mu_e\tau_e) \end{aligned} \quad (46)$$

where we define  $p = p_i + p_e$  and  $\mathbf{j} = ne(\mathbf{v}_i - \mathbf{v}_e)$ .

Since  $\mathbf{j} \times \mathbf{B} = \frac{1}{\mu_o}(\nabla \times \mathbf{B}) \times \mathbf{B} = -\frac{1}{\mu_o} \nabla \cdot (-\mathbf{B}\mathbf{B}^t + \frac{1}{2}|\mathbf{B}|^2\mathbf{I})$ , the combined 'single-fluid momentum conservation equation' is obtained as following,

$$\frac{\partial(\rho\mathbf{v})}{\partial t} = -\nabla \cdot (\rho\mathbf{v}\mathbf{v}^t - \frac{\mathbf{B}\mathbf{B}^t}{\mu_o} + (p + \frac{1}{2\mu_o}|\mathbf{B}|^2)\mathbf{I} - \mu_i\tau_i - \mu_e\tau_e) \quad (47)$$

After non-dimensionalization, we have:

$$\frac{\partial(\rho\mathbf{v})}{\partial t} = -\nabla \cdot (\rho\mathbf{v}\mathbf{v}^t - \mathbf{B}\mathbf{B}^t + (p + \frac{1}{2}|\mathbf{B}|^2)\mathbf{I} - \frac{1}{S_{vi}}\tau_i - \frac{1}{S_{ve}}\tau_e) \quad (48)$$

where  $S_{vi} = \frac{\rho_o V_A L_o}{\mu_i}$  and  $S_{ve} = \frac{\rho_o V_A L_o}{\mu_e}$ .

## Magnetic Field

$$\frac{\partial \mathbf{B}}{\partial t} = -\nabla \times \mathbf{E} \quad (49)$$

where  $\mathbf{E} = \frac{1}{\sigma\mu_o} \nabla \times \mathbf{B} - \mathbf{v} \times \mathbf{B}$ .

$$\frac{\partial \mathbf{B}}{\partial t} = -\nabla \times (\mathbf{B} \times \mathbf{v} + \frac{1}{\sigma\mu_o} \nabla \times \mathbf{B}) \quad (50)$$

where  $\mathbf{v} = \frac{M\mathbf{v}_i + m\mathbf{v}_e}{M+m}$ . After non-dimensionalization, we have,

$$\frac{\partial \mathbf{B}}{\partial t} = -\nabla \times (\mathbf{B} \times \mathbf{v} + \frac{1}{S_r} \nabla \times \mathbf{B}) \quad (51)$$

where  $S_r = \mu_o V_A L_o / \eta$ .

## Energy conservation

In two-fluids plasma energy conservation equations, we have:

$$\frac{\partial E_i}{\partial t} + \nabla \cdot [(E_i + p_i)\mathbf{v}_i] = \mathbf{j}_i \cdot \mathbf{E} + \nabla \cdot (\mu_i \mathbf{v}_i \cdot \boldsymbol{\tau}_i + \kappa_i \nabla T_i) \quad (52)$$

$$\frac{\partial E_e}{\partial t} + \nabla \cdot [(E_e + p_e)\mathbf{v}_e] = \mathbf{j}_e \cdot \mathbf{E} + \nabla \cdot (\mu_e \mathbf{v}_e \cdot \boldsymbol{\tau}_e + \kappa_e \nabla T_e) \quad (53)$$

By substituting  $\mathbf{v}_i \approx \mathbf{v} + \frac{m\mathbf{j}}{Mne}$  and  $\mathbf{v}_e \approx \mathbf{v} - \frac{\mathbf{j}}{ne}$  into the above two equations, we have:

$$\begin{aligned} \frac{\partial E_i}{\partial t} + \nabla \cdot [(E_i + p_i)\mathbf{v}] + \frac{m}{M\mu_o ne} \nabla \cdot [(E_i + p_i)(\nabla \times \mathbf{B})] &= \\ \mathbf{j}_i \cdot \mathbf{E} + \nabla \cdot (\mu_i \mathbf{v}_i \cdot \boldsymbol{\tau}_i + \kappa_i \nabla T_i) & \end{aligned} \quad (54)$$

$$\begin{aligned} \frac{\partial E_e}{\partial t} + \nabla \cdot [(E_e + p_e)\mathbf{v}] - \frac{1}{\mu_o ne} \nabla \cdot [(E_e + p_e)(\nabla \times \mathbf{B})] &= \\ \mathbf{j}_e \cdot \mathbf{E} + \nabla \cdot (\mu_e \mathbf{v}_e \cdot \boldsymbol{\tau}_e + \kappa_e \nabla T_e) & \end{aligned} \quad (55)$$

Adding the above two equations and considering in two-dimensional space,  $\nabla \cdot (\nabla \times \mathbf{B}) = 0$ , the above equation can be simplified as:

$$\begin{aligned} \frac{\partial E_{tot}}{\partial t} + \nabla \cdot [(E_{tot} + p)\mathbf{v}] &= \mathbf{j} \cdot \mathbf{E} \\ + \nabla \cdot (\mu_i \mathbf{v}_i \cdot \boldsymbol{\tau}_i + \mu_e \mathbf{v}_e \cdot \boldsymbol{\tau}_e + \kappa_i \nabla T_i + \kappa_e \nabla T_e) & \end{aligned} \quad (56)$$

Using the magnetic field equation obtained above, we have:

$$\begin{aligned} \frac{1}{2} \frac{\partial \mathbf{B}^2}{\partial t} &= -\mathbf{B} \cdot \nabla \times (\mathbf{B} \times \mathbf{v} + \eta \nabla \times \mathbf{B}) \\ &= -\nabla \cdot [(\frac{1}{2} |\mathbf{B}|^2 I - \mathbf{B}\mathbf{B}^t) \cdot \mathbf{v} + \eta \mathbf{j} \times \mathbf{B}] - \mathbf{j} \cdot \mathbf{E} \end{aligned} \quad (57)$$

Adding the above two equations, we have:

$$\begin{aligned} \frac{\partial E_{tot}}{\partial t} + \nabla \cdot [(E_{tot} + p)\mathbf{v}] &= \mathbf{j} \cdot \mathbf{E} + \nabla \cdot (\mu_i \mathbf{v}_i \cdot \boldsymbol{\tau}_i + \mu_e \mathbf{v}_e \cdot \boldsymbol{\tau}_e + k_i \nabla T_i + k_e \nabla T_e) \\ &- \nabla \cdot [(\frac{1}{2}|\mathbf{B}|^2 I - \mathbf{B}\mathbf{B}^t) \cdot \mathbf{v} + \eta \mathbf{j} \times \mathbf{B}] - \mathbf{j} \cdot \mathbf{E} \end{aligned} \quad (58)$$

Since

$$(\nabla \times \mathbf{B}) \times \mathbf{B} = \mathbf{B} \cdot \nabla \mathbf{B} - \nabla \frac{|\mathbf{B}|^2}{2} \quad (59)$$

We have the combined energy conservation equation:

$$\begin{aligned} \frac{\partial E_{tot}}{\partial t} &= -\nabla \cdot [(E_{tot} + p)\mathbf{v} + (\frac{1}{2}|\mathbf{B}|^2 I - \mathbf{B}\mathbf{B}^t) \cdot \mathbf{v} - \mu_i \mathbf{v} \cdot \boldsymbol{\tau}_i - \mu_e \mathbf{v} \cdot \boldsymbol{\tau}_e \\ &- k_i \nabla T_i - k_e \nabla T_e + \eta(\mathbf{B} \cdot \nabla \mathbf{B} - \nabla \frac{|\mathbf{B}|^2}{2})] \end{aligned} \quad (60)$$

After non-dimensionalization, we have,

$$\begin{aligned} \frac{\partial E_{tot}}{\partial t} &= -\nabla \cdot [(E_{tot} + p)\mathbf{v} + (\frac{1}{2}|\mathbf{B}|^2 I - \mathbf{B}\mathbf{B}^t) \cdot \mathbf{v} - \frac{\gamma}{S_{vi}Pr_i} \nabla T_i - \frac{\gamma}{S_{ve}Pr_e} \nabla T_e \\ &- \frac{1}{S_{vi}} \mathbf{v} \cdot \boldsymbol{\tau}_i - \frac{1}{S_{ve}} \mathbf{v} \cdot \boldsymbol{\tau}_e + \frac{1}{S_r} (\mathbf{B} \cdot \nabla \mathbf{B} - \nabla \frac{|\mathbf{B}|^2}{2})] \end{aligned} \quad (61)$$

where  $Pr_i = \frac{C_p \mu_i}{\kappa_i}$  and  $Pr_e = \frac{C_p \mu_e}{\kappa_e}$ .

## Electron energy conservation

The electron energy conservation equation is:

$$\frac{\partial \epsilon_e}{\partial t} + \nabla \cdot [(\epsilon_e + p_e)\mathbf{v}_e] = \nabla \cdot (\kappa_e \nabla T_e) + \mu_e \boldsymbol{\tau}_e : \nabla \mathbf{v}_e + \mathbf{v}_e \cdot \nabla p_e + \eta \mathbf{j} \cdot \mathbf{j} \quad (62)$$

By substituting  $\mathbf{v}_e \approx \mathbf{v} - \frac{\mathbf{j}}{ne}$  into above equation, we have:

$$\begin{aligned} \frac{\partial \epsilon_e}{\partial t} &+ \nabla \cdot [(\epsilon_e + p_e)\mathbf{v}] - \frac{1}{\mu_o ne} \nabla \cdot [(\epsilon_e + p_e)(\nabla \times \mathbf{B})] \\ &= \nabla \cdot (\kappa_e \nabla T_e) + \mu_e \boldsymbol{\tau}_e : \nabla \mathbf{v}_e + \mathbf{v} \cdot \nabla p_e - \frac{(\nabla \times \mathbf{B})}{\mu_o ne} \cdot \nabla p_e + \eta \mathbf{j} \cdot \mathbf{j} \end{aligned} \quad (63)$$

Considering the two-dimensional space,  $\nabla \cdot (\nabla \times \mathbf{B}) = 0$  and  $\frac{(\nabla \times \mathbf{B})}{\mu_0 n e} \cdot \nabla p_e = 0$ , above equation can be simplified:

$$\begin{aligned} \frac{\partial \epsilon_e}{\partial t} + \nabla \cdot [(\epsilon_e + p_e) \mathbf{v}] \\ = \nabla \cdot (\kappa_e \nabla T_e) + \mu_e \tau_e : \nabla \mathbf{v} + \mathbf{v} \cdot \nabla p_e + \eta \mathbf{j} \cdot \mathbf{j} \end{aligned} \quad (64)$$

After non-dimensionalization, we have,

$$\begin{aligned} \frac{\partial \epsilon_e}{\partial t} = & -\nabla \cdot [(\epsilon_e + p_e) \mathbf{v} - \frac{\gamma}{S_{ve} Pr_e} \nabla T_e] \\ & + \mathbf{v} \cdot \nabla p_e + \frac{1}{S_{ve}} \tau_e : \nabla \mathbf{v} + \frac{1}{S_r} (\nabla \times \mathbf{B}) \cdot (\nabla \times \mathbf{B}) \end{aligned} \quad (65)$$

### ACKNOWLEDGEMENTS

This work was supported by the computational mathematics program of AFOSR. We would like to acknowledge helpful discussions with Prof. N. Gatsonis regarding this work. Computations were performed at NPACI's SP3.

## References

- [1] N. A. Gatsonis and X. Yin. Hybrid (particle/fluid) modeling of pulsed plasma thruster plumes. *Journal of Spacecraft and Rockets*, 17:945–958, 2001.
- [2] N. A. Gatsonis, R.A. Nanson, and G.J. Le Beau. Simulations of cold-gas nozzle and plume flows and flight data comparisons. *Journal of Spacecraft and Rockets*, 37:39–48, 2000.
- [3] W. Dai and P.R. Woodward. A simple Riemann solver and high-order Godunov schemes for hyperbolic systems of conservation laws. *Journal of Computational Physics*, 121:51, 1995.
- [4] A.L. Zachary, A. Malagoli, and P. Colella. A higher-order Godunov method for multidimensional ideal magnetohydrodynamics. *SIAM J. Sci. Stat Comp.*, 15:15, 1994.

- [5] R.E. Peterkin, M.H. Frese, and C.R. Sovinec. Transport magnetic flux in an arbitrary coordinate ALE code. *Journal of Computational Physics*, 140:148, 1998.
- [6] K.G. Powell. An approximate Riemann solver for magnetohydrodynamics (that works in more than one dimension). *ICASE Report No. 94-24*, 1994.
- [7] O.S. Jones, U. Shumlak, and D.S. Eberhardt. An implicit scheme for nonideal magnetohydrodynamics. *J. Comput. Phys.*, 130:231, 1997.
- [8] P. Colella, M. Dorr, and D.D. Wake. A conservative finite difference method for the numerical solution of plasma fluid equations. *Technical Report UCRL-JC-129912*, 1998.
- [9] P.J. Turchi and P.G. Mikellides. Modeling of ablation-fed pulsed plasma thrusters. *31th AIAA/ASME/SAE/ASEE Joint Propulsion Conference and Exhibit*, July 10-12 1995.
- [10] U. Shumlak and B. Udrea. An approximate Riemann solver for MHD computations on parallel architectures. In *AIAA 2001-2591, 15th AIAA Computational Fluid Dynamics Conference*, Anaheim, CA, June 11-14 2001.
- [11] J.P. Freidber. Ideal magnetohydrodynamic theory of magnetic fusion systems. *Reviews of Modern Physics*, 54(3):801, 1982.
- [12] U. Shumlak and J. Loverich. Approximate Riemann solver for the two-fluid plasma model. *J. Comp. Phys.*, 187:620, 2003.
- [13] R.T. Brown and M. Mitchner. Measurements of a nonequilibrium plasma boundary layer. *Physics of Fluids*, 14(5):933, 1971.
- [14] J.R. Roth and D.M. Sherman. Boundary layer flow control with a one atmosphere uniform glow discharge surface plasma. In *AIAA 98-0328, 36th Aerospace Sciences Meeting & Exhibit*, Reno, NV, January 12-15 1998.
- [15] S.P. Wilkinson. Investigation of an oscillating surface plasma for turbulent drag reduction. In *AIAA 2003-1023, 41st Aerospace Sciences Meeting & Exhibit*, Reno, NV, January 6-9 2003.

- [16] T.C. Warburton and G.E. Karniadakis. A discontinuous Galerkin method for the viscous MHD equations. *J. Comput. Phys.*, 152:608, 1999.
- [17] R.B. Dahlburg and J.M. Picone. Evolution of the Orszag-Tang vortex system in a compressible medium. I. Initial average subsonic flow. *Phys. Fluids B*, 1(11), 1989.
- [18] H.O. Kreiss and J. Olinger. *Methods for the approximate solution of time-dependent problems*. GARP Publ. Ser. vol. 10, GARP, Geneva, 1973.
- [19] D.V. Gaitonde. High-order solution procedure for three-dimensional nonideal magnetogasdynamics. *AIAA J.*, 39(11):2111, 2001.
- [20] D.V. Gaitonde and J. Poggie. Elements of a numerical procedure for 3-D MGD flow control analysis. In *AIAA 2002-0198, 40th Aerospace Sciences Meeting & Exhibit*, Reno, NV, January 14-17 2002.
- [21] A.H. Glasser and X.Z. Tang. Progress in the development of the SEL macroscopic modeling code. In *Sherwood Fusion Theory Conference*, Corpu Christi, TX, April 28-30 2003.
- [22] B. Cockburn, G.E. Karniadakis, and C.-W. Shu. The development of Discontinuous Galerkin methods. In *Discontinuous Galerkin Methods: Theory, Computation and Applications*. Springer, 2000.
- [23] C.R. Evans and J.F. Hawley. Simulation of magnetohydrodynamic flows: A constrained transport method. *Astro. Phys. J.*, 332:659–677, 1988.
- [24] G.E. Karniadakis and S.J. Sherwin. *Spectral/hp Element Methods for CFD*. Oxford University Press, 1999.
- [25] K. F. Gurski. An hllc-type approximate Riemann solver for ideal magnetohydrodynamics. *SIAM Journal of Scientific Computing*, 25:2165–2187, 2004.
- [26] J.U. Brackbill and D.C. Barnes. The effect of nonzero  $\nabla \cdot \mathbf{b}$  on the numerical solution of the magnetohydrodynamic equations. *J. Comput. Phys.*, 35:426, 1980.

- [27] P. Janhunen. A positive conservative method for magnetohydrodynamics based on HLL and Roe methods. *Journal of Computational Physics*, 160:649–661, 2000.
- [28] K. G. Powell, P. L. Roe, R. S. Myong, T. I. Gombosi, and D. L. DeZeeuw. An upwind scheme for magnetohydrodynamics. *AIAA 12th Computational Dynamics Conference*, San Diego, CA, page 661, AIAA-95-1704, 1995.
- [29] E. Priest. Solar magnetohydrodynamics. *D. Reidel Publishing Company*, 1982.
- [30] M. Mitchner and C. H. Kruger Jr. Partially ionized gases. *John Wiley & Sons, Inc.*, 1973.
- [31] M. Brio and C.C. Wu. An upwind differencing scheme for the equations of ideal magnetohydrodynamics. *J. Comput. Phys.*, 75:400, 1988.